ALMA REVEALS THE ANATOMY OF THE mm-SIZED DUST AND MOLECULAR GAS IN THE HD 97048 DISK

Catherine Walsh[1,2], Attila Juhász[3], Gwendolyn Meeus[4], William R. F. Dent[5], Luke T. Maud[1],
Yuri Aikawa[6], Tom J. Millar[7], and Hideko Nomura[8]

[1] Leiden Observatory, Leiden University, P.O. Box 9531, 2300 RA Leiden, The Netherlands; cwalsh@strw.leidenuniv.nl, c.walsh1@leeds.ac.uk
[2] School of Physics and Astronomy, University of Leeds, Leeds LS2 9JT, UK
[3] Institute of Astronomy, University of Cambridge, Madingley Road, Cambridge CB3 0HA, UK
[4] Departamento de Física Teórica, Universidad Autonoma de Madrid, Campus Cantoblanco, E-28049 Madrid, Spain
[5] Joint ALMA Observatory (JAO), Alonso de Córdova 3107, Vitacura, Santiago, Chile
[6] Center for Computer Sciences, University of Tsukuba, 305-8577 Tsukuba, Japan
[7] School of Mathematics and Physics, Queen's University Belfast, University Road, Belfast BT7 1NN, UK
[8] Department of Earth and Planetary Science, Tokyo Institute of Technology, 2-12-1 Ookayama, Meguro-ku, 152-8551 Tokyo, Japan

ABSTRACT

Transitional disks show a lack of excess emission at infrared wavelengths due to a large dust cavity, that is often corroborated by spatially resolved observations at $\sim$ mm wavelengths. We present the first spatially resolved $\sim$ mm-wavelength images of the disk around the Herbig Ae/Be star, HD 97048. Scattered light images show that the disk extends to $\approx$640 au. ALMA data reveal a circular-symmetric dusty disk extending to $\approx$350 au, and a molecular disk traced in CO $J = 3$-2 emission, extending to $\approx$750 au. The CO emission arises from a flared layer with an opening angle $\approx$30°–40°. HD 97048 is another source for which the large ($\sim$ mm-sized) dust grains are more centrally concentrated than the small ($\sim\mu$m-sized) grains and molecular gas, likely due to radial drift. The images and visibility data modeling suggest a decrement in continuum emission within $\approx$50 au, consistent with the cavity size determined from mid-infrared imaging (34 ± 4 au). The extracted continuum intensity profiles show ring-like structures with peaks at $\approx$50, 150, and 300 au, with associated gaps at $\approx$100 and 250 au. This structure should be confirmed in higher-resolution images (FWHM $\approx$ 10–20 au). These data confirm the classification of HD 97048 as a transitional disk that also possesses multiple ring-like structures in the dust continuum emission. Additional data are required at multiple and well-separated frequencies to fully characterize the disk structure, and thereby constrain the mechanism(s) responsible for sculpting the HD 97048 disk.

Key words: protoplanetary disks – stars: individual (HD 97048) – stars: pre-main sequence – submillimeter: planetary systems

1. INTRODUCTION

Protoplanetary disks are the sites of planetary system formation. So-called *transitional disks* are considered a particular class of protoplanetary disk which have substantial dust cavities (or gaps, see the recent review by Espaillat et al. 2014). The origin of dust cavities in transitional disks is much debated in the literature. Theories range from photo-evaporation of dust and gas by the central star (see, e.g., Alexander et al. 2014) to the development of *dead zones*, regions of low ionization which impede the angular momentum and mass transport leading to the build-up of material in a ring-like structure (Regály et al. 2013; Flock et al. 2015). A third theory is that unseen massive planets or companions in the disk create steep pressure gradients in the gas, which shepherd large dust grains into rings (so-called "dust traps"), generating the appearance of a large cavity when imaged at (sub-)mm wavelengths (Andrews et al. 2011; Pinilla et al. 2012a). Distinguishing between theories requires complementary observations of the molecular gas and imaging of the emission from both small ($\sim\mu$m) and large ($\sim$ mm) dust grains (see Table 2 in Espaillat et al. 2014). Cavities in both dust (small and large) and gas are likely created by photoevaporation whereas those created by pressure bumps (possibly triggered by planets) are devoid of large (mm) grains only, and residual gas and small dust grains may remain (due to dust filtration, see, e.g., Rice et al. 2006).

Transitional disks were originally identified via the lack of near- to mid-infrared (IR) emission in the spectral energy distributions (SEDs) of disk-hosting stars, indicating a depletion in warm dust and hence, the presence of an inner dust cavity (see, e.g., Strom et al. 1989). Several transitional disks encompass Herbig Ae/Be (HAeBe) stars ($T_{\rm eff}$, $\sim$10,000 K, Waters & Waelkens 1998). HAeBe star–disk systems have been further classified by the shape of the SEDs in the mid-IR into either Group I or Group II disks; the former have a flared structure (driven by absorption of stellar UV photons) and the latter are considered to be "flat" disks (Meeus et al. 2001), within which the dust has grown to mm-sizes, has become decoupled from the gas, and has settled to the midplane (Dullemond & Dominik 2004). This scenario of the gradual depletion of small dust grains which absorbs the UV radiation necessary to trigger the flared structure has led to speculation in the literature that Group II disks may be a later evolutionary state of Group I disks (Dullemond & Dominik 2004). The advent of interferometric imaging across the wavelength range of interest has thrown doubt on this rather intuitive evolutionary scenario. High spatial-resolution imaging at long ($\gtrsim$mm) wavelengths with ALMA, JVLA, and ATCA have revealed that grain growth can already be advanced in Group I disks ($\beta \lesssim 1$, where $F_\nu \propto \nu^{\beta+2}$), e.g., HD 142527 (Casassus et al. 2013, 2015), IRS 48 (van der Marel et al. 2013, 2015), and HD 100546 (Pineda et al. 2014; Walsh et al. 2014; Wright et al. 2015). It should be noted that the value of β is also sensitive to grain composition (Draine 2006). Recent mid-IR imaging also suggests that all Group I disks are transitional in nature, and the resulting flared structure is therefore linked to

the presence of the inner cavity (Honda et al. 2012; Maaskant et al. 2013). Assuming the theory that massive planets are responsible for generating such cavities, perhaps primordial protoplanetary disks follow one of two evolutionary paths with the division into Group I or Group II, dependent upon the formation of a massive companion (and associated cavity) early in the disk lifetime (see, e.g., Currie & Kenyon 2014). The picture is further complicated by recent mid-IR interferometric observations which suggest that several Group II HAeBe disks also exhibit evidence of inner cavities, albeit smaller than those typically seen in Group I disks (Menu et al. 2015). These authors hypothesize that the Group II objects are younger, and the evolution into a Group I disk follows the formation of an inner cavity.

It is clear that complementary observations across the wavelength range of interest, from near-IR to (sub-)mm, are necessary to help further elucidate the evolutionary paths and states of HAeBe disks and the physical origin of the cavities observed therein. We present spatially resolved ALMA Cycle 0 observations of the Group I HAeBe star–disk system, HD 97048. The observations reveal for the first time the spatial distribution of the large ($\sim$ mm-sized) dust grains and molecular gas in this otherwise well-studied source. In Sections 2–5 we describe the source, the observations, present our results, and discuss the implications, respectively.

2. THE SOURCE: HD 97048

HD 97048 is a Herbig Ae/Be star with spectral type B9–A0 ($T_\star \approx 10{,}000$ K) and a mass of 2.5 $M_\odot$, located in the Chameleon I star-forming region at a distance of ≈ 160 pc (van den Ancker et al. 1998; van Leeuwen 2007). To date, the HD 97048 star–disk system has been well studied at short wavelengths only. Early observations from 2.0 to 4.0 μm with the Anglo-Australian Telescope revealed strong emission features between 3.3 and 3.6 μm (Blades & Whittet 1980). Later observations with the *Infrared Space Observatory* revealed additional emission at 6.2, 7.7, 8.6, and 11.3 μm, attributed to polyaromatic hydrocarbons (PAHs, Gürtler et al. 1999; van Kerckhoven et al. 2002). Mid-IR imaging showed extended PAH emission (out to several hundred au) in line with that predicted by flared protoplanetary disk models (van Boekel et al. 2004; Lagage et al. 2006; Doucet et al. 2007; Mariñas et al. 2011). The lack of any silicate features in the IR spectra suggested that the opacity is dominated by small carbonaceous dust grains, a property supported by more recent data from *Spitzer* (Acke et al. 2010; Juhász et al. 2010). Scattered light images at optical wavelengths using the *Hubble Space Telescope*/Advanced Camera for Surveys revealed the radial extent of the small dust grains, ≈ 640 au (assuming a source distance of 160 pc), and evidence of filamentary structures postulated to be spiral arms (Doering et al. 2007). PDI (polarimetric differential imaging) images with VLT/ NACO in the H and K_s bands (1.66 and 2.18 μm, respectively) revealed the innermost dust (16–160 au, Quanz et al. 2012). However, recent fits to the SED and azimuthally averaged mid-IR brightness profile (Q-band, 24.5 μm) unearthed the potential transitional nature of HD 97048 for the first time (Maaskant et al. 2013). The authors find that the SED and brightness profile are best fit with a dust cavity 34 $\pm$ 4 au in radius and also infer the presence of an inner, optically thick, dusty disk between 0.3 and 2.5 au.

Regarding the gas, detection of the [O I] line at 6300 Å uncovered an inner rotating gas disk (Acke & van den Ancker 2006). High-spectral resolution observations of CO rovibrational emission revealed a significant reservoir of warm molecular gas in Keplerian motion within ≈ 100 au (van der Plas et al. 2009, 2015). van der Plas et al. (2009) also infer a cavity in the inner CO reservoir of 11 au, suggesting efficient photodissociation of CO by the harsh stellar radiation field. There is also evidence that HD 97048 hosts a gas-rich outer disk: H$_2$ emission has been detected by numerous groups (Martin-Zaïdi et al. 2007, 2009; Bary et al. 2008; Carmona et al. 2011) allowing estimates on the spatial extent of the warm gas (out to a few 10 s of au). HD 97048 was also a target in two *Herschel* Open Time Key Programs dedicated to characterizing the gas in protoplanetary disks, GASPS (P.I., W. R. F. Dent) and DIGIT (P.I., N. J. Evans). Meeus et al. (2012, 2013) and Fedele et al. (2013) reported PACS detections of line emission from [O I] at 63.18 and 145.53 μm and from [C II] at 157.75 μm. Also detected were several high-J rotational lines of CO (ranging from $J = 15$-14 to $J = 30$-29), multiple lines of OH, and two rotational transitions of CH$^+$ ($J = 6$-5 and 5-4). van der Wiel et al. (2014) report additional detections ($>3\sigma$) of CO rotational line emission (from $J = 9$-8 to $J = 13$-12) with SPIRE.

Despite being well-studied at shorter wavelengths, there is a lack of data at (sub-)mm wavelengths. Henning et al. (1994) detected continuum emission at 1.3 mm using the SEST 15 m telescope measuring a flux of 451.5 $\pm$ 34 mJy. Follow-up mapping showed that the emission was compact, although at that time it had not yet been inferred that this source hosted a protoplanetary disk (Henning et al. 1998). More recent LABOCA (The Large Apex BOlometer CAmera) observations determined a flux of 2610 $\pm$ 131 mJy at 870 μm (Phillips 2010). Hales et al. (2014) report emission from the CO $J = 3$-2 line (346 GHz) toward HD 97048 in an APEX survey of nearby T Tauri and Herbig Ae stars; however, they conclude that the line emission is heavily contaminated by emission from the background Chameleon I molecular cloud, based upon an assumption for the source velocity obtained from Carmona et al. (2011). Very recently, Kama et al. (2016) conducted an APEX survey of [CI]^{3}P$_1$ $-^3$ P$_0$ (492.161 GHz), [CI]^{3}P$_2$ $-^3$ P$_1$ (809.342 GHz) and CO $J = 6$-5 (691.473 GHz) line emission from a sample of nearby protoplanetary disks (33 sources in total). All three lines were detected toward HD 97048, with this source having the brightest intrinsic line emission compared with all other sources in the sample. HD 97048 was also one of the brightest emitters in all far-IR emission lines in the *Herschel* PACS data (Meeus et al. 2012, 2013; Fedele et al. 2013), making this one of the brightest known disks to date in sub-mm line emission. All data discussed thus far have been conducted with single-dish telescopes and thus are spatially unresolved. The ALMA data presented here are the first to spatially resolve both the dust emission and the molecular disk at (sub-)mm wavelengths.

3. OBSERVATIONS

HD 97048 was observed with 25 antennas in a compact configuration during ALMA Cycle 0 operations on 2012 December 14 (program 2011.0.00863.S, P.I. C. Walsh). Baselines ranged from 15.1 to 402 m and the target was observed in seven spectral windows centered at 300.506, 301.286, 303.927, 344.311, 345.798, 346.998, and

347.331 GHz. The channel width was 122.070 kHz corresponding to 0.12 km s^{-1} at 302 GHz and 0.11 km s^{-1} at 346 GHz; hence, the spectral resolution, applying Hanning smoothing, was 0.24 and 0.22 km s^{-1}, respectively, The total on-source time was 24 minutes 17 s for the first execution (at the lower frequency) and 23 minutes 59 s for the second execution (at the higher frequency). The quasars J0522-364 and J1147-6753 were used as bandpass and phase calibrators, respectively, and Callisto was used as amplitude calibrator for the data at ≈302 GHz. For the data at the higher frequency (≈346 GHz), the quasar 3c279 was used as bandpass and amplitude calibrator, and J1147-6753 was used as phase calibrator.

Upon inspection of the delivered data at ≈346 GHz, it was discovered that, due to the lack of a specified flux calibrator observation, the flux scaling had not been set in the initial calibration; hence, we recalibrated the raw data using 3c279 as the flux calibrator. 3c279 had not been monitored regularly in Band 7 during the time of our observations with the nearest data taken more than two months either side of the date at which our data were taken. As a solution, we used the two Band 3 monitoring measurements at ≈98 and ≈110 GHz taken just three days before our observations to calculate the spectral index of 3c279 and thus bootstrap the Band 3 flux to our Band 7 data (using the ALMA Analysis Utilities[9] task, GetALMA-Flux[10]). This reported the spectral index for 3c279 as 0.73 ± 0.01 and the flux at Band 7 (346 GHz) as 8.86 ± 0.51 Jy. Although this corresponds to a flux uncertainty of ≈5%, considering the variable spectral index of 3c279 (for instance, the next monitoring observations taken two months later indicate that the spectral index becomes shallower), we estimate a total error on the flux of the source at 346 GHz as closer to ≈15%, but this could be underestimated.

The data were self-calibrated using CASA version 4.3, during which several antennas were flagged reducing the total number of antennas to 22. We used the continuum data at each respective wavelength to self-calibrate all data (continuum and lines) before final imaging. We used a timescale of 20 s (corresponding to ≈3 times the integration step), and increased the dynamic range of the continuum data by a factor of ≈20. After removal of line-containing channels and edge channels, the total available continuum bandwidth amounted to 1.39 GHz at 302 GHz (993 μm) and 1.86 GHz at 346 GHz (866 μm). Having two essentially independent observations at different frequencies allowed us to assess the reality of low-level features in the data.

4. RESULTS

4.1. Continuum Emission

4.1.1. Continuum Images

In Figure 1, we display the continuum emission at 302 and 346 GHz imaged using the CLEAN[11] algorithm with Briggs weighting (robust = 0.5, top panels). This resulted in synthesized beams of 0″.88 × 0″.52 (−43°.9) at 302 GHz and 0″.69 × 0″.43 (−23°.2) at 346 GHz. The elliptical beams are due to the relatively low decl. of the source (−77°) and the antenna configuration. The resulting images have highest

---

spatial resolution in the north-east–south-west direction. The respective rms noise is 0.34 and 0.36 mJy/beam. The signal-to-noise level reached in the images is 1220 at the lower frequency and 880 at the higher frequency. The contour levels displayed in the figure are 3, 10, 30, 100, and 300 times the rms noise. Additionally, the 1000σ contour is shown for the 302 GHz continuum and the 600σ contour shown for the 346 GHz continuum.

The total continuum flux density is 2.14 and 2.23 Jy at 302 and 346 GHz, respectively. Using the flux measured at $\nu = 302$ GHz and assuming that the continuum emission is optically thin, the total dust mass, $M_{\rm dust}$, can be estimated as

$$M_{\rm dust} = \frac{D^2 F_\nu}{\kappa_\nu B_\nu(T_{\rm dust})}, \tag{1}$$

where D is the source distance (160 pc), κ_ν is the dust mass opacity at a frequency, ν, and B_ν the value of the Planck function for dust temperature, $T_{\rm dust}$. For $\kappa_\nu = 5$ cm^2 g^{-1} and a dust temperature of 30 K (Beckwith et al. 1990; Andrews et al. 2011), this suggests a total dust mass of 1.3×10^{30} g which corresponds to 0.70 $M_{\rm Jup}$. Because HD 97048 is a Herbig Ae star, the dust temperature in the outer disk could be higher than 30 K; hence, this estimate is an upper limit to the total dust mass for the assumed dust mass opacity.

The two fluxes measured by ALMA (2.14 and 2.23 Jy at 302 and 346 GHz, respectively) imply a very shallow spectral index for the continuum emission ($\alpha = 0.30 \pm 0.03$, where $F_\nu \propto \nu^\alpha$). This also suggests that the emission is highly optically thick at these frequencies, meaning that the primary assumption made in deriving the dust mass estimate no longer holds. However, given the issues with the flux calibration of the data at 346 GHz data detailed in Section 3, it is possible that we have underestimated the error on the flux at this frequency. We leave a more robust determination of the spectral index of the dust emission (and also the dust mass) to future work using data at higher spatial resolution and additional data at lower frequencies.

The images in Figure 1 show a spatially resolved and extended dusty disk at least 2″ in radius, corresponding to at least 320 au, assuming a distance to source of 160 pc. As a first step in characterizing the system, the CASA task uvmodel-fit[12] was used to fit the continuum visibilities assuming that the emission arises from an elliptical disk. The two measurement sets (at 302 and 346 GHz) were fit independently and resulted in almost identical disk parameters: a disk radius of 2″.2 (350 au), an inclination of 41°, and a position angle (P.A.) of 3°. The fit also confirmed that the phase center of the data is at the expected source position. The fitted P.A. is consistent with the images: an inclined disk with a P.A. close to 0° will naturally appear elongated in the north–south direction relative to the east–west direction. The images and fitting also confirm that the continuum emission is arising predominantly from the disk midplane because the aspect ratio is that expected for an ellipse centered at the source position with the disk P.A. and inclination. On the other hand, emission from a flared surface from such an inclined disk with P.A. ≈ 0 would show an extension in emission toward the east relative to the west (see, e.g., Lagage et al. 2006). The disk inclination is in good agreement with previous estimates derived from mid-IR and
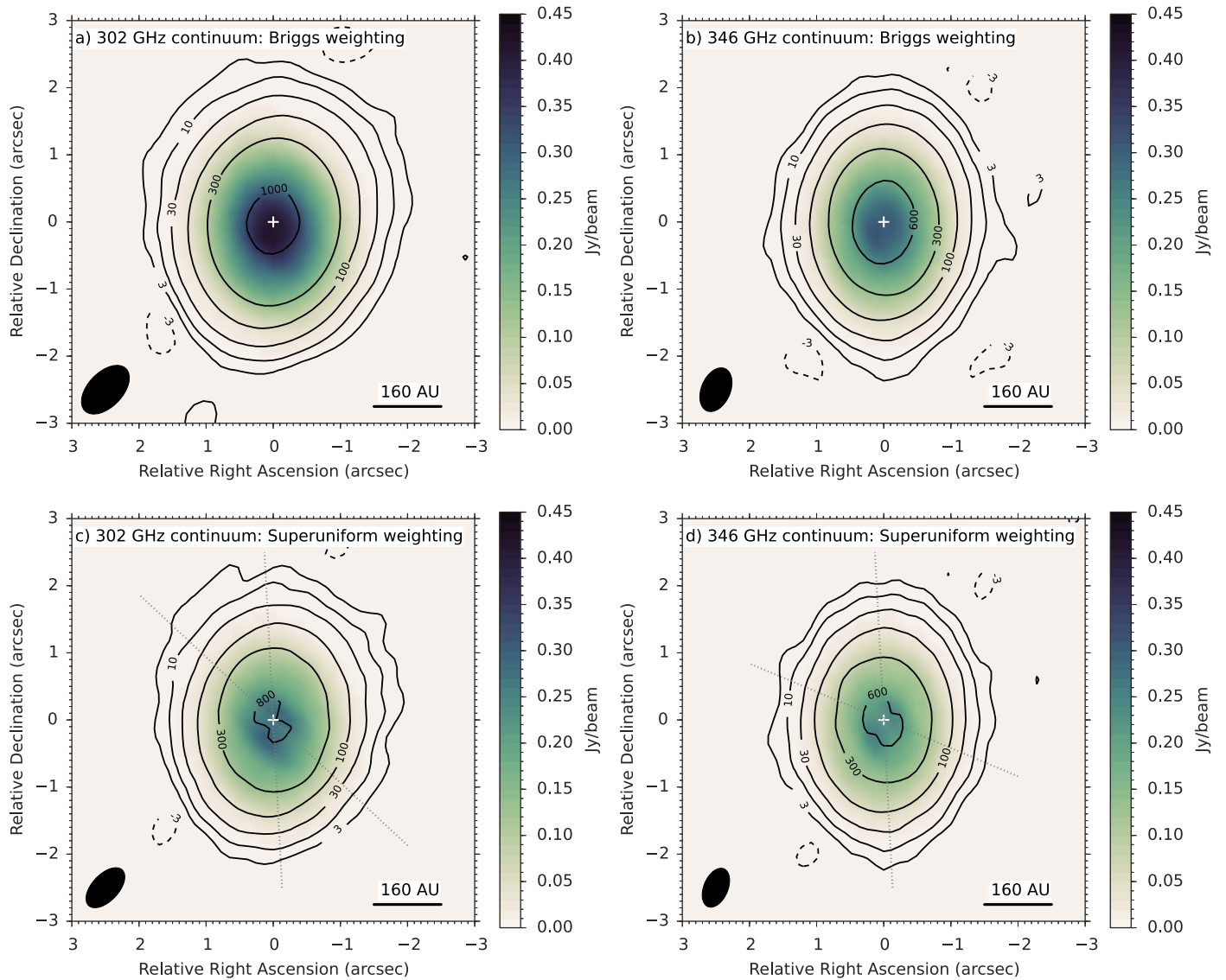

Figure 1. ALMA Cycle 0 continuum images of the disk surrounding HD 97048 at 302 GHz (left-hand panels) and 346 GHz (right-hand panels), CLEANed using Briggs weighting (top row) and superuniform weighting (bottom row). The synthesized beam sizes are listed in the main text. The white cross indicates the source position. The dotted gray lines in the bottom two panels show the slices across the disk major axis (3°) and the beam minor axes (47° and 67° at 302 and 346 GHz, respectively). The contour levels are in σ, where $1\sigma = 0.34$ and 0.36 mJy, respectively.

PDI images (Lagage et al. 2006; Quanz et al. 2012). Previous determinations of the P.A. of the disk (east of north) range from $160° \pm 19°$ (Acke & van den Ancker 2006) to $78° \pm 10°$ (Quanz et al. 2012). These values differ somewhat from that determined here; however, the observations from which the P. A. is derived are more sensitive to the inner disk. As discussed in Quanz et al. (2012), it is possible for both the inner disk geometry and the dust properties to differ from those in the outer disk. Although never quantified, the mid-IR images also suggest a position angle close to 0° on the sky (Lagage et al. 2006; Doucet et al. 2007; Mariñas et al. 2011).

In the images presented in the top panels of Figure 1 there is no indication of a gap in the disk nor any hint of additional structure. The maximum spatial resolution achieved in the images (set by the size of the minor axis of the synthesized beam) is equivalent to 83 au at 302 GHz and 69 au at 346 GHz, assuming a distance to source of 160 pc. Given that the proposed size of the cavity in the inner disk from mid-IR imaging is 34 ± 4 au in radius (Maaskant et al. 2013), the

image resolution is just beyond that required to detect an equivalent-sized gap in the (sub-)mm images. The use of Briggs weighting in the CLEAN algorithm is a compromise between sensitivity to large scale emission and spatial resolution (natural versus uniform weighting, respectively; Briggs 1995). Because the signal-to-noise level of the images is high, we can apply the uniform weighting scheme in the CLEAN algorithm which gives higher resolution at the expense of a reduced signal-to-noise (see, e.g., Isella et al. 2012). In the bottom panels of Figure 1, we present the resulting images using superuniform weighting. This has the added effect that the side lobes are further suppressed, allowing better sensitivity on the largest scales compared with uniform weighting (Briggs 1995). The resulting synthesized beam sizes are $0\rlap{.}''73 \times 0\rlap{.}''40$ $(-43°3)$ and $0\rlap{.}''61 \times 0\rlap{.}''36$ $(-23°0)$ at 302 and 346 GHz respectively. The spatial resolution is increased to 64 au for the 302 GHz continuum and 58 au for the 346 GHz continuum. The images now show the signature of a gap (or at least a reduction) in the emission on small scales indicated by
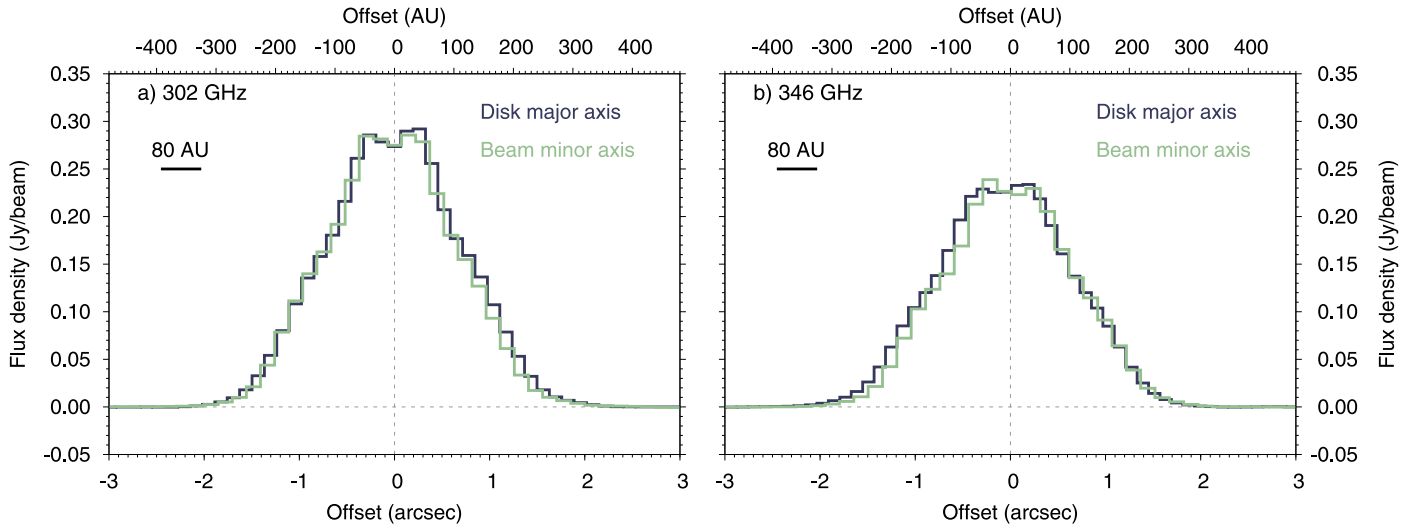
Figure 2. Continuum flux density at 302 GHz (left-hand panel) and 346 GHz (right-hand panel) along a slice across the disk major axis (3°, dark blue lines) and beam minor axes (47° and 67° at 302 and 346 GHz, respectively, light green lines).

the shapes of the 800σ and 600σ contours at 302 and 346 GHz, respectively. The "hour-glass"-shaped innermost contours, which are aligned with the beam minor axis along which the spatial resolution is highest, show that the peak of the emission is offset from the source position (indicated by the white cross; see also Hughes et al. 2007; Andrews et al. 2011).

In Figure 2, we display slices through the continuum images generated using superuniform weighting along the disk major axis (3°, dark blue lines) and along the beam minor axes at each frequency (light green lines). For the latter data, the offset has been scaled to account for the disk inclination (41°) and the respective position angle of the beams.[13] A positive offset indicates the direction of increasing decl. and R.A. The slices are indicated by the dashed gray lines in the bottom panels of Figure 1. All slices show a flattening and/or reduction in flux at the position of the source, again showing that the continuum emission peaks at a position offset from the source center.

4.1.2. Continuum Visibilities

We conduct all subsequent analysis of the continuum emission in the visibility domain. This allows extraction of information about the disk structure on spatial scales smoothed over in the reconstructed images. Whether the continuum emission originates from a disk with a dust-depleted inner cavity (i.e., a ring), as suggested in the images with superuniform weighting, can be tested by examining the visibilities. For a circular-symmetric brightness distribution from a ring, the real components of the visibilities will show a null (zero crossing) and the imaginary components will be close to zero (see, e.g., Hughes et al. 2007; Walsh et al. 2014). In Figure 3, we display the visibilities for HD 97048 which have been rotated and deprojected using the disk inclination and P.A. determined from the ALMA data (41° and 3°, respectively). The top panels show the real components and the bottom panels show the imaginary components, both binned into 10 kλ-sized bins. The error bars shown correspond to the

standard error of the mean and are generally smaller than the point size. The real components show a shallow null at ≈150 kλ indicating that the emission may arise from a ring. This is better seen in the inset plots which zoom into the region specified by the dashed gray box in the main plot. The imaginary components show small scatter about zero, confirming that the continuum emission is close to circular symmetric. On the longest baselines ($\gtrsim$250 kλ), the imaginary components begin to deviate from zero. This is most apparent in the higher signal-to-noise data at 302 GHz. However, the magnitude of the largest imaginary components is on the order of 20% of the real components; hence, for the most part, the emission arises from a circular symmetric disk.

4.1.3. Continuum Modeling

To quantify the morphology of the disk we model the brightness distribution using simple analytical functions. The real components of the visibilities are then calculated given that the intensity distribution can be treated as a summation over infinitesimally narrow rings, the Fourier transform for which is a zeroth-order Bessel function of the first kind (J_0, Berger & Segransan 2007). The real components are thus given by,

$$V_{\mathrm{Re}}(\rho) = 2\pi \int_0^\infty I(r) \, J_0(2\pi \, r \, \rho) \, r \, dr, \qquad (2)$$

where ρ is the baseline grid (for which the binned data grid was used). Any circular-symmetric intensity distribution, $I(r)$, can be inserted into this equation to compute the corresponding real components of the visibilities. Note that we do not attempt to decouple the dust surface density and temperature profiles because to do so would introduce significant degeneracies in the models. To break such degeneracies requires spatially resolved continuum observations at two well-separated frequencies and even then, assumptions have to be made regarding the dust opacity (see, e.g., Andrews & Williams 2007; Guilloteau et al. 2011). We leave characterization of the dust density and temperature distribution to future work at higher resolutions.

---

[13] $(r/a) = \cos i/\sqrt{\sin^2\alpha + \cos^2\alpha \cos^2 i}$ where r is the projected radius of the disk along the minor axis of the beam, a is the disk major axis (assumed aligned in the north–south direction), i is the disk inclination, and α is the angle of the minor axis of the beam, measured east from north.
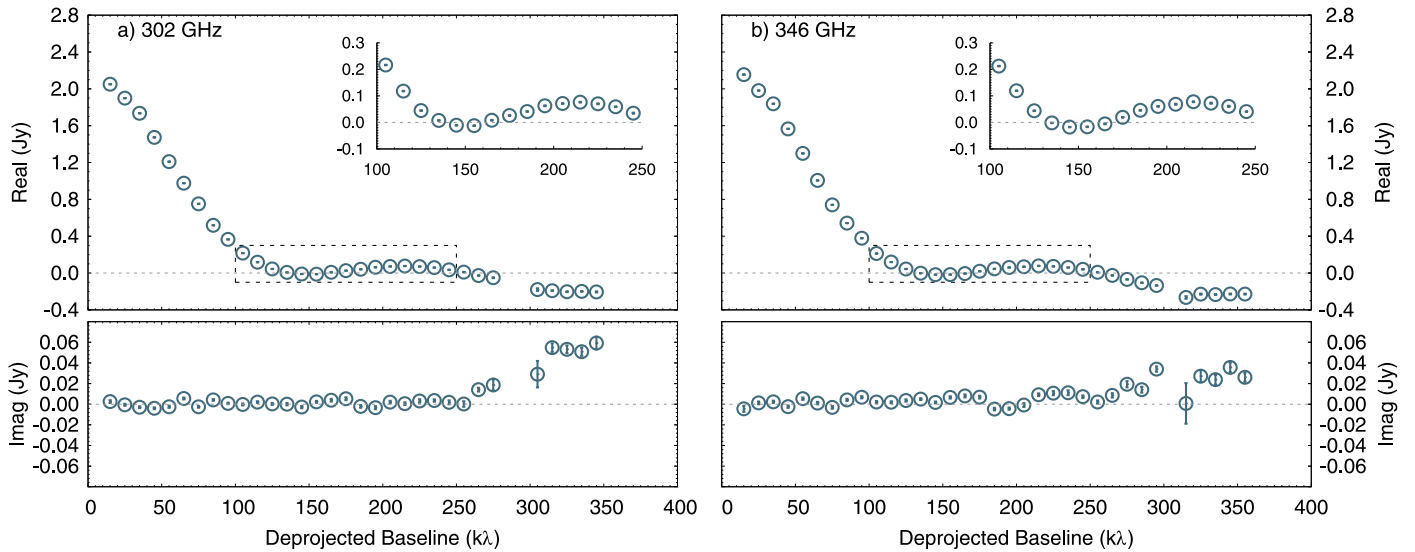
Figure 3. Real and imaginary components of the visibilities (top and bottom, respectively) at 302 GHz (left-hand panels) and 346 GHz (right-hand panels). The data are binned to 10 kλ-sized bins and the error bars correspond to the standard error of the mean in each bin. Note that the error bars are, in general, smaller than the size of the points. The inset plots show a zoom of the region enclosed by the dashed gray box.

To extract the intensity profiles at both frequencies from the binned and deprojected visibilities, we use the method recently proposed by Zhang et al. (2016). This involves modeling the intensity distribution as a summation over Gaussians (each with an amplitude, a_i, and a width, σ_i) modulated by a sinusoidal function with a spatial frequency, ρ_i. The underlying intensity distribution is assumed to also be a Gaussian function with a width, σ_0. This technique is powerful because it allows the addition of substructure (including peaks and troughs) with various spatial frequencies, while also ensuring that the intensity tends to 0 at infinity. Using this method, Zhang et al. (2016) were able to recover the intensity profile in four protoplanetary disks recently imaged at moderate ($\approx 0\rlap{.}''2$–$0\rlap{.}''4$) to high ($\approx 0\rlap{.}''02$–$0\rlap{.}''03$) angular resolution. A particular highlight is that they recover the major features of the intensity profile of the dust emission from HL Tau, using only baselines $\lesssim 2000$ kλ. The produced image, on the other hand, was created using baselines $\lesssim 12{,}000$ kλ (ALMA Partnership et al. 2015). Further details on the methodology can be found in Zhang et al. (2016).

The radial intensity profile is given by

$$I_n(r) = \frac{a_0}{\sqrt{2\pi}\,\sigma_0} \exp\left(-\frac{r^2}{2\sigma_0^2}\right) + \sum_{i=1}^{n} \cos(2\pi r \rho_i)$$
$$\times \frac{a_i}{\sqrt{2\pi}\,\sigma_i} \exp\left(-\frac{r^2}{2\sigma_i^2}\right). \qquad (3)$$

Zhang et al. (2016) use the Levenburg–Marquardt χ^2 minimization technique to fit their intensity profiles. Because this technique is prone to getting stuck in local minima unless a good starting point is found, we opt to use the Markov Chain Monte Carlo (MCMC) approach coupled with Bayesian statistics, to determine the best-fit intensity profile, $I_n(r)$, for a given number of Gaussian components, n. A radial grid of 10 au resolution was deemed sufficient to model the data. The Python module, pymc[14], was used (Patil et al. 2010). We

assume all prior distributions for the fitted parameters, $[a_i, \sigma_i, \rho_i]$, are uniform with boundaries set by the range of radii and spatial frequencies probed by the continuum data ($\lesssim 500$ au and $\lesssim 500$ kλ, respectively). The intensity profiles are also scaled to the observations using the observed flux at both frequencies, which are assumed to have a normal distribution with a standard deviation of 10% at 302 GHz and 15% at 346 GHz.

Our modeling approach is now described and is similar to that conducted by Zhang et al. (2016). First, a single Gaussian intensity profile is fitted, I_0, to determine the best-fit Gaussian width, σ_0, and to test whether this is an adequate fit to the data. Additional single Gaussian components are then systematically added to the fit, using the best-fit parameters from the previous model (because MCMC models also benefit from a good starting point). The addition of components is halted when an incremental improvement in the real residuals of the visibilities is found. We also go one step further than Zhang et al. (2016) and display the residuals from the model fitting in both the real components of the visibilities, and the corresponding residual images.

It is found that two additional Gaussian components only are required (i.e., I_2) to reproduce the visibility data at both frequencies. Figure 4 shows the resulting visibility profiles at both frequencies and respective real residuals. The model fits give an excellent "by-eye" fit to the visibility data: quantitatively, the fits are also good, with peak residuals on the order of ≈ 20–30 mJy (corresponding to $\approx 1\%$ of the total flux density). Figure 5 shows the imaged residuals at 302 and 345 GHz. The peak residuals are 16 and 23 mJy/beam, respectively, which correspond to 4% and 7% of the peak flux density in the observed images. The maximum imaged residuals are also close to, and offset from, the source position. This could be due to emission arising from the innermost regions which is not well described using a circular-symmetric intensity profile. That the imaginary components deviate from zero on the longest baselines (also visible in the unbinned data) is also possible evidence of non-axisymmetric emission on small scales (see Figure 3). Furthermore, the total flux densities in the

---
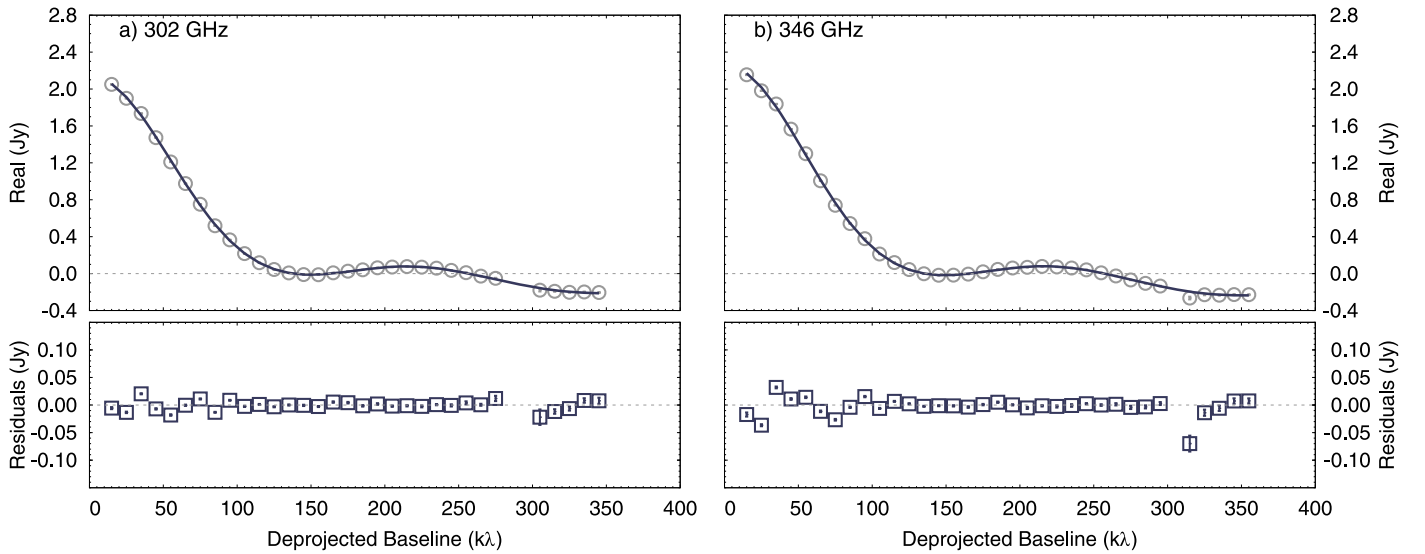
Figure 4. Real components of the visibilities for the best-fit intensity profiles (dark blue lines) and respective real residuals as a function of deprojected baseline. The observed binned and deprojected visibilities are plotted in gray circles.

imaged residuals are 8.0 and 26 mJy/beam, so that the models reproduce ≈99% of the observed fluxes (2.14 and 2.23 Jy, respectively).

In Figure 6 we show the extracted and normalized intensity profile for the 302 GHz data at the model grid resolution (10 au, light green solid lines), and convolved with a 20 au beam (dotted gray lines) and a 50 au beam (dashed dark blue lines) on both a linear (left) and a logarithmic (right) intensity scale. The dashed horizontal line on the logarithmic plot represents the normalized 3σ rms continuum noise at 302 GHz. The respective plots for the 346 GHz data fits are very similar and so are not displayed. The fits to the visibility profile predict the presence of two peaks in the radial intensity profile at ≈50 and 150 au, and a third "shoulder" at ≈250–300 au is evident in the logarithmic plot. The model fits also suggest a decrement in (sub-)mm continuum emission within ≈50 au, confirming the classification of this disk as a transition disk, as well as gaps at ≈100 and 250 au. We note that we tried a more complex model with an additional central component to attempt to quantify the decrement in emission within the cavity; however, the improvement in fit was not significant, and higher spatial resolution data are needed to further guide the models. We emphasize here that the recovery of this substructure is only possible due to the high signal-to-noise of the data ($\gtrsim$1000) and the direct modeling of the visibility data.

4.2. CO J = 3-2 Line Emission

4.2.1. Channel Maps and Line Profile

The CO J = 3-2 (345.796 GHz) emission was extracted from the full self-calibrated measurement set and then continuum subtracted in the *uv*-plane using the CASA task `uvcontsub`.[15] The CO emission was then imaged using CLEAN with Briggs weighting (robust = 0.5), with a slight oversampling in velocity resolution (0.15 km s^{-1}). The resulting synthesized beam is 0″69 × 0″44 (−23°.2). Masking was done interactively on a channel-per-channel basis. Emission was detected across ≈100 velocity channels ranging from

−2.70 to 12.3 km s^{-1}. The resulting rms noise is 18.1 mJy/beam in the channels, and the peak signal-to-noise is 122.

In Figure 7, the CO J = 3-2 (345.796 GHz) channel maps (shifted by the source velocity) are displayed. The maps show a spatially resolved and inclined and flared disk, with blueshifted emission from the south side of the disk and redshifted emission from the north side. The maps confirm that the disk is inclined toward the east relative to the disk major axis (P.A. 3°), and is rotating in a counter-clockwise direction. This is in agreement with the disk rotation direction determined via analysis of [O I] line emission at 6300 Å (Acke & van den Ancker 2006). Line emission is suppressed or missing in velocity channels from −1.20 to 0.90 km s^{-1} inclusive. This could be due to absorption by foreground material (the observed extinction toward HD 97048 is 1.24 mag, van den Ancker et al. 1998), or spatial filtering of extended emission from background material. HD 97048 is in close proximity to the Chameleon I molecular cloud.

Even though HD 97048 lies in a region of bright extended emission, these data are sufficiently high quality to constrain the source velocity ($V_{\mathrm{LSRK}} = 4.65 \pm 0.075$ km s^{-1}, relative to the Kinematic Local Standard of Rest). In Figure 8 we show the line profile generated summing all emission within a polygon, the shape of which is determined by the extent of the emission in all directions out to the 3σ contour of the integrated intensity. The shaded region corresponds to those velocity channels affected by foreground absorption and/or spatial filtering. The line profile has been mirrored and shifted (gray lines) to confirm the determination of the source velocity from these data (indicated by the central vertical gray dashed line), despite the missing emission at, and around, the source systemic velocity.

4.2.2. The Radius of the Molecular Disk

In Figure 9, we compare the CO J = 3-2 first moment map (corrected by the source velocity) with the integrated intensity (dashed gray contours at 3, 10, 30, 100, and 150σ) and the 3σ continuum extent (dashed black contour). The first moment map was generated using a conservative clip at a 5σ level, whereas the integrated intensity (or zeroth moment map) was

---

[15] http://casa.nrao.edu/docs/taskref/uvcontsub-task.html
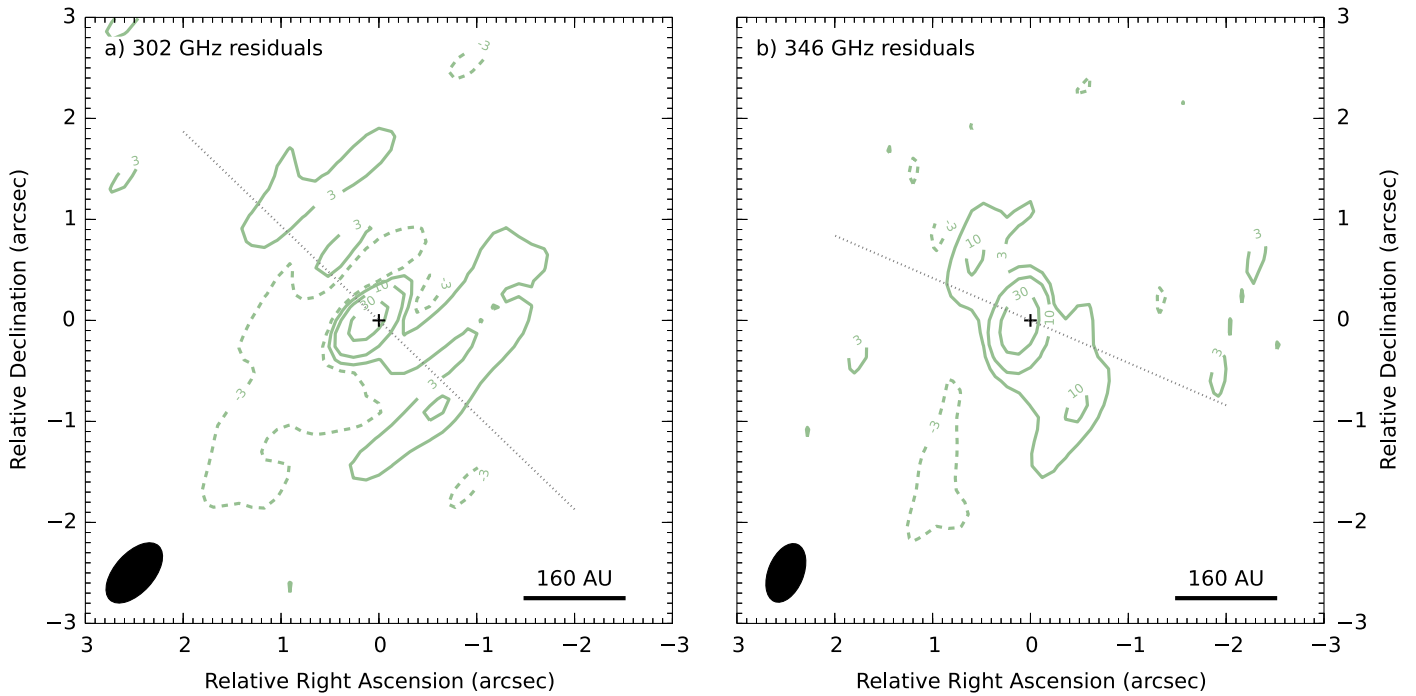
Figure 5. Real residuals imaged with superuniform weighting at 302 GHz (left-hand panels) and at 346 GHz (right-hand panels) for the best-fit intensity profiles. The black cross indicates the source (or stellar) position. The dotted gray lines show the slices across the beam minor axes ($47°$ and $67°$ at 302 and 346 GHz, respectively). The contour levels are in σ, where $1\sigma = 0.34$ and 0.36 mJy, respectively.

generated by summing over all channels in the data cube with all pixels with a value $<3\sigma$ masked. We estimate the rms noise level in the integrated intensity as 25.3 mJy km s^{-1} calculated by summing over *all* channels (87 in total) containing emission at a level $\geqslant 3\sigma$ ($\sqrt{n}\,\sigma\Delta v$, where n is the number of channels, σ is the rms noise per channel, and Δv is the channel width). It is this value that is used to compute the dashed gray contours in Figure 9.

The strange "dumbbell" shape in the integrated intensity and first moment maps is because of the missing emission at and around the source velocity. The emission along the minor axis of the disk (east–west direction) is most affected, whereas that along the major axis (north–south direction) is least affected because it is in this direction that the projected velocity along the line of sight is largest. There is also evidence that emission from the largest spatial scales may also be affected because the extent of the northern redshifted emission is larger than that of the southern blueshifted emission which is consistent with the range of velocities most affected by foreground absorption and/or spatial filtering (-1.20 to 0.90 km s^{-1}, see Figures 7 and 8). Hence, in all subsequent analysis, it is only possible to determine a lower limit to the spatial extent of the molecular disk. Line emission from relatively abundant and optically thin isotopologues (e.g., ^{13}CO or C^{18}O), and/or higher energy rotational transitions of ^{12}CO, may help to confirm the radial extent of the molecular disk.

Figure 9 shows that the molecular disk extends to at least $\approx 4''$. This is more extended than the continuum at 346 GHz ($\approx 2''$). In Figure 10, we compare the CO integrated intensity and continuum emission at 346 GHz, both normalized by their peak value, along the disk major axis. The horizontal dashed lines show the respective 3σ rms noise levels. This plot clearly shows that the disk is significantly more extended in CO line emission. Similar to the initial analysis conducted for the

continuum, we use the CASA task `uvmodelfit` to model the integrated intensity of the line emission as arising from a geometrically thin disk to refine the estimation of the disk radius. This gives a result for the radius of $>4\rlap{.}''7$ corresponding to >750 au, making this disk one of the largest known in ^{12}CO molecular emission. The disk extent imaged in scattered light at optical wavelengths suggests an outer radius of ≈ 640 au assuming a source distance of 160 pc (Doering et al. 2007). Hence, it is likely that the ALMA data are probing the full spatial extent of the molecular disk despite the missing emission at and around the source velocity. These data also allow us to confirm that the extended emission seen in scattered light does indeed arise from a circumstellar disk, as opposed to a remnant circumstellar envelope as proposed as an alternative explanation by Doering et al. (2007).

The ^{12}CO integrated intensity suggests that the molecular disk is at least twice as large in radial extent as the (sub-)mm dust disk which is possible evidence of radial drift of large ($\sim$mm-sized) dust grains; however, extraction of the (sub-)mm dust and CO radial column densities are needed to confirm that the gas-to-dust mass ratio does indeed increase in the outermost regions of the disk. The alternative explanation is that emission external to ≈ 350 au from (sub-)mm dust simply falls below the sensitivity limits of the current data. Extraction of CO column densities is difficult to do using ^{12}CO alone because the emission is optically thick and arises from the uppermost layers in the disk, and observations of optically thin emission from isotopologues are necessary. Furthermore, extraction of column densities requires a well-constrained radial and vertical temperature structure. Due to the lack of spatially resolved data, especially at (sub-)mm wavelengths, this does not yet exist for the disk around HD 97048.

Alternatively, the continuum rms noise level in the outermost regions can be used to estimate an upper limit to the
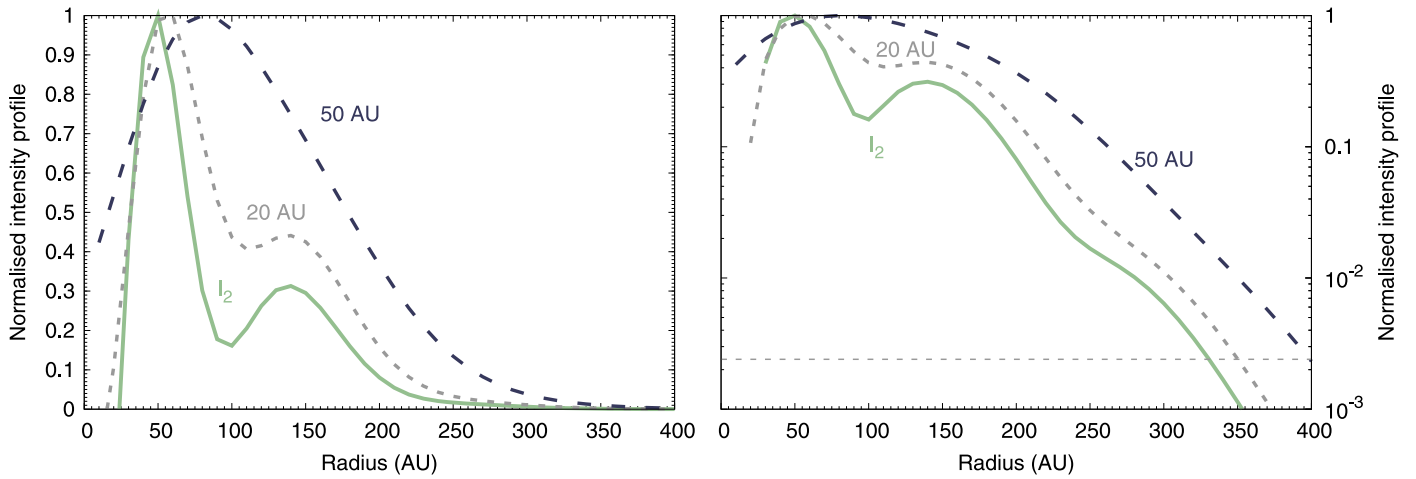
Figure 6. Normalized continuum intensity profiles as a function of radius for the best-fit intensity profile at the model grid resolution (light green solid lines) and convolved with a 20 au beam (gray dotted lines) and a 50 au beam (dark blue dashed lines). The horizontal dashed gray line in the right-hand panel signifies the 3σ rms continuum noise at 302 GHz (relative to the peak intensity).

unseen dust mass, and thus to the dust mass surface density. The dust mass, $M_{\mathrm{dust}}^{\mathrm{out}}$ can be estimated using Equation (1): at $\nu = 302$ GHz, the rms noise is 0.34 mJy beam^{-1} which gives an annulus-integrated continuum flux density of $F_{\nu}^{\mathrm{out}} \approx 40$ mJy between 2″2 (350 au) and 4″7 (750 au). Assuming a dust opacity, $\kappa_{\nu} = 5$ g cm^{-2}, and a conservative dust temperature, $T_{\mathrm{dust}} = 30$ K (see, e.g., Beckwith et al. 1990; Andrews et al. 2011) gives a total unseen dust mass, $M_{\mathrm{dust}}^{\mathrm{out}} < 2.5 \times 10^{28}$ g. Assuming that the column density is constant over this outer annulus gives an upper limit to the dust column density of $\Sigma_{\mathrm{dust}}^{\mathrm{out}} \approx 8 \times 10^{-5}$ g cm^{-2}. Given that it is likely that the dust emission continues to decrease as a function of radius toward the outer disk, this is a very conservative upper limit. For the canonical gas-to-dust mass ratio of ~ 100, this implies a gas mass column density of $\Sigma_{\mathrm{gas}}^{\mathrm{out}} < 8 \times 10^{-3}$ g cm^{-2} (assuming integration in the vertical direction orthogonal to the disk midplane) which corresponds to a gas number column density of $\lesssim 2 \times 10^{21}$ cm^{-2} for a mean molecular mass of 2.2 amu (i.e., 90% H$_2$ and 10% He). This gas column density is approaching that required for efficient self and mutual shielding of CO from photodissociation by photons from the central star and/or interstellar medium (see, e.g., Visser et al. 2009). The simple "back-of-the-envelope" calculation done here implies that the gas-to-dust mass ratio in the outer disk is *at least* the canonical value of ~ 100 to allow CO to survive with a sufficient abundance to large radii. That the ^{12}CO emission also originates from layers high up in the disk atmosphere (see the next section) provides additional evidence that the gas-to-dust mass ratio in the outer regions is likely significantly higher than the canonical value, because CO is already able to reach its shielding column at large geometrical heights in the disk. Given that the temperature structure of the outermost regions of this disk is not yet well constrained, it is possible that this emission morphology can also be attributed to CO freeze-out in the disk midplane. However, we do not see a clear decrement in emission between the front and back side of the disk (due to a lack of CO emission from the midplane, see Figure 7), which has been seen for disks which do possess this morphology due to CO freeze-out, e.g., HD 163296 (De Gregorio-Monsalvo et al. 2013). Spatially resolved observations of optically thin tracers will confirm which scenario holds.

4.2.3. Constraining the Flaring Angle of the CO-emitting Layer

The CO $J = 3$-2 channel maps (Figure 7) suggest that the CO emission arises from a flared disk. For inclined and flared disks, the back side of the disk can become visible in the channel maps: this is possible because the line-of-sight projected velocities at the same radius from the front and back side will be offset from each other (see, e.g., Sememov et al. 2007; De Gregorio-Monsalvo et al. 2013; Rosenfeld et al. 2013). The back side of the disk is potentially visible in channels from 0.90 to 1.65 km s^{-1} which also show that the CO emission arises from a layer at a particularly large geometrical height.

As a first attempt to constrain the opening angle (relative to the midplane) of the CO-emitting layer, we plot the channel maps mirroring the positive and negative channels at the same velocity (from ± 0.75 to ± 1.80 km s^{-1}, Figure 11). The line emission arises from a layer clearly angled toward the east (in the direction of increasing R.A.) relative to that expected for an inclined geometrically flat disk. Also overlaid on the mirrored channel maps are the projected angles of a layer inclined at 41° relative to the disk P.A. (3°) for an opening angle of 30°, 35°, and 40° (white dotted lines, with the angle increasing from right to left). Further refinement of the opening angle without detailed modeling (such as that conducted by Rosenfeld et al. 2013 and beyond the scope of this work) is difficult because of the lack of emission in and around the source velocity. This simple geometrical analysis shows that the opening angle of CO-emitting layer is $\approx 35° \pm 5°$ confirming the flared nature of this protoplanetary disk.

In the previous section, we derived the radius of the molecular disk by assuming that the emission arises from a geometrically thin disk and modeling the CO $J = 3$-2 integrated intensity in the uv plane. That the CO arises from a layer which is significantly inclined with respect to the midplane should not affect the determination of the disk radius by this method, since the projected radius of the flared layer will coincide with the radial extent of the disk along the midplane.
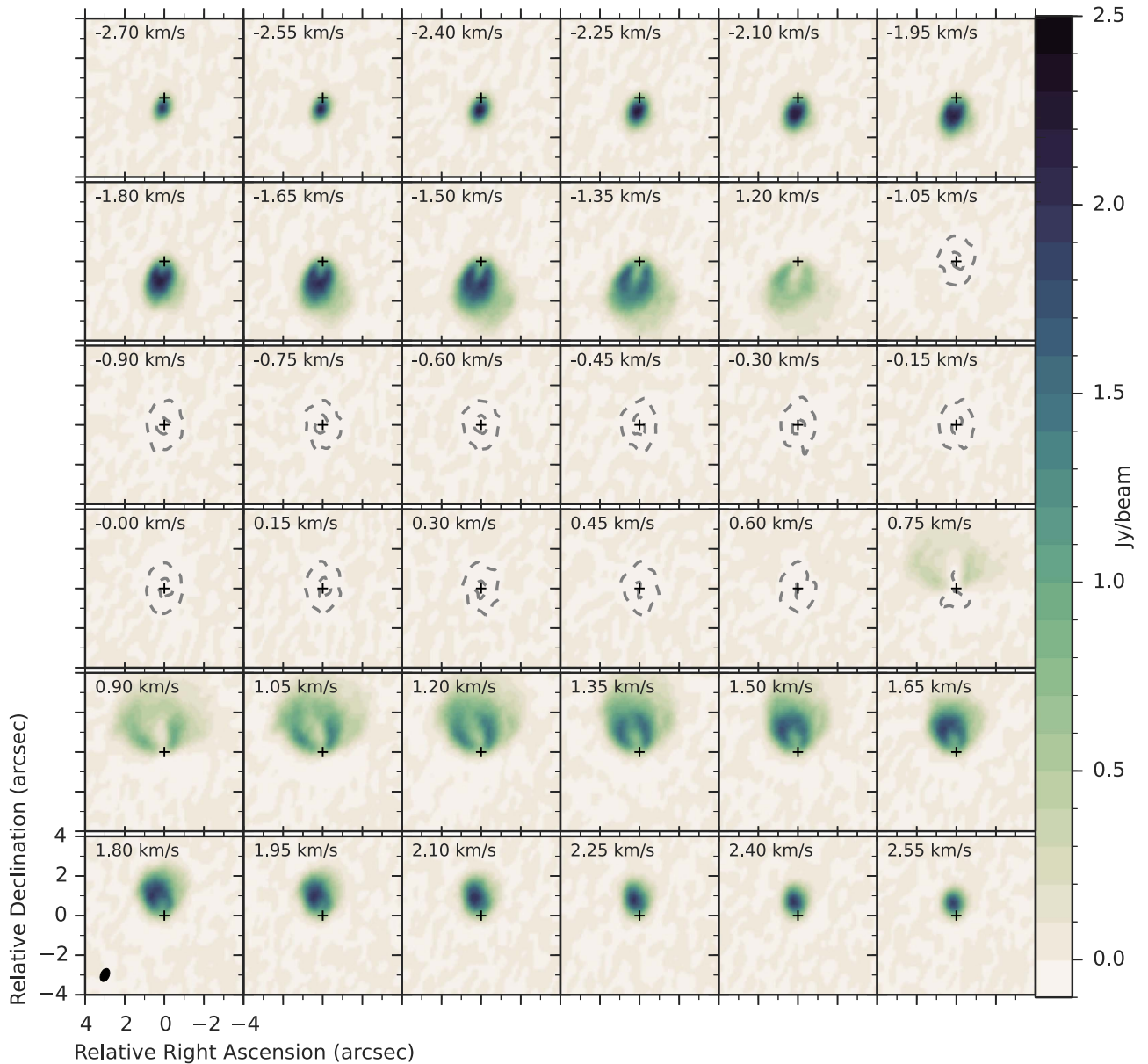
Figure 7. Channel maps showing the CO $J = 3\text{-}2$ (345.796 GHz) line emission. The missing emission from -1.20 to 0.90 km s^{-1} inclusive may be due to absorption by foreground material and/or spatial filtering of extended background material. The black cross indicates the source position and the synthesized beam is shown in the bottom left-hand corner of the bottom left-hand panel. Note that the source velocity (4.65 km s^{-1}) has been subtracted from these data.

5. DISCUSSION

5.1. On the Transitional Nature of HD 97048

The data presented here support the proposed transitional nature of the disk encompassing HD 97048, with the data and extracted intensity profile showing a decrement in continuum emission within ≈ 50 au. The data also show that the molecular gas and small (μm-sized) dust grains have a larger radial extent than the large (mm-sized) dust grains (750 au versus 350 au). Better data are needed to quantify the dust depletion factor within the identified cavity. This discrepancy in radial extent between the (sub-)mm-sized dust and molecular gas may be indicative of dust evolution during the disk lifetime: as dust grains grow, they become decoupled from the gas, feel a headwind from the slightly sub-Keplerian gas, and move inwards to conserve angular momentum, a process termed *radial drift* (see, e.g., Whipple 1972; Weidenschilling 1997).

This has been seen in several other disks imaged at (sub-)mm wavelengths at relatively high spatial resolution ($\lesssim 0''.5$), including TW Hya (Andrews et al. 2012, 2016; Hogerheijde et al. 2016), LkCa 15 (Isella et al. 2012), HD 163296 (Isella et al. 2009; De Gregorio-Monsalvo et al. 2013), and HD 100546 (Pineda et al. 2014; Walsh et al. 2014). Sharply truncated dust disks are predicted by dust evolution models which simulate radial drift coupled with viscous gas drag (Birnstiel & Andrews 2014). Birnstiel & Andrews (2014) predict that the radius of (sub-)mm dust disks can decrease to values as low as $1/4$–$1/3$ that of the gaseous disk by 10^6 years. Such "sharp" outer edges are found to form quickly during early stages in the disk lifetime ($\sim 10^5$ year) and can persist to late stages ($\sim 10^6$ year) if the drift becomes "self-limited," i.e., as dust is lost to the star, the dust-to-gas mass ratio decreases, and the maximum achievable particle size reduces (Birnstiel & Andrews 2014). HD 97048 is considered a rather young
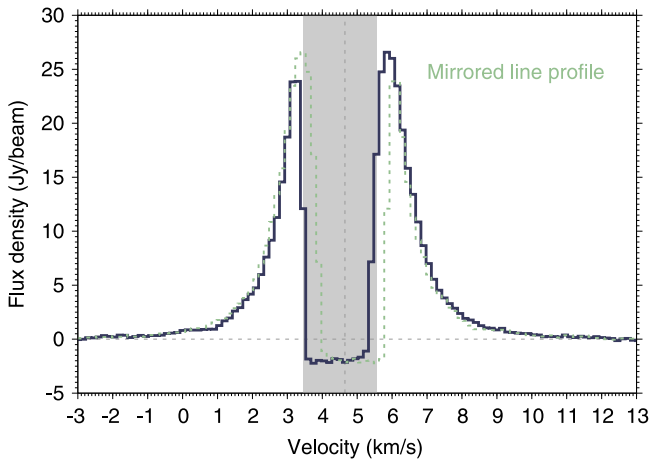
Figure 8. CO $J = 3$-2 (345.796 GHz) line profile generated from a polygon containing all emission within the maximum extent of the 3σ contour. The mirrored line profile is given by the dotted light greeni lines. The source velocity (V_{LSRK}) determined from this data is 4.65 ± 0.075 km s^{-1}.
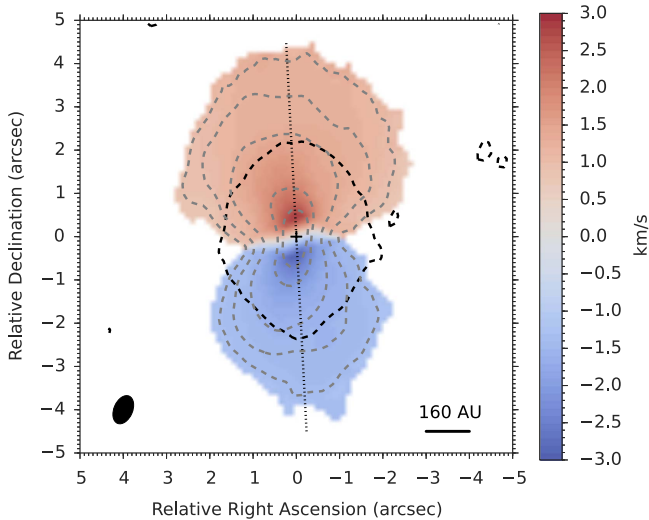
Figure 9. CO $J = 3$-2 (345.796 GHz) first moment map (color map) and integrated intensity contours (dashed gray lines) compared with the 3σ contour for the continuum at 346 GHz (dashed black line). The 3, 10, 30, 100, and 150σ contours are shown for the integrated intensity. The dotted gray line shows the slice across the disk major axis ($3°$).
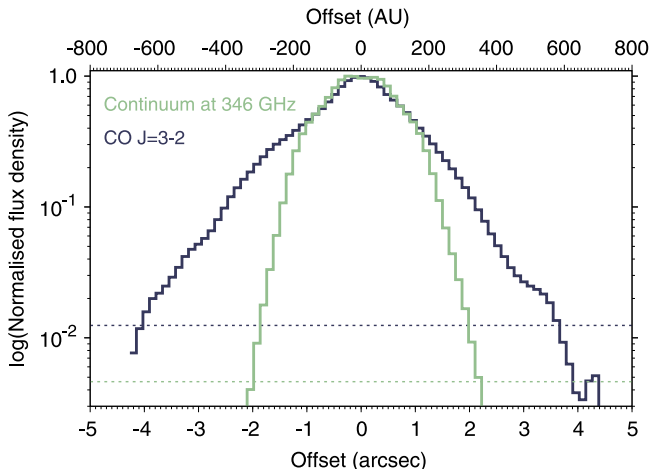
Figure 10. Normalized CO $J = 3$-2 (345.796 GHz) integrated intensity (dark blue) and 346 GHz continuum emission (light green) along the disk major axis. The dashed horizontal lines represent the respective 3σ rms noise levels.

source, with an estimated age of $\approx$2–3 Myr (van den Ancker et al. 1998; Lagage et al. 2006; Doering et al. 2007; Martin-Zaïdi et al. 2009). The ALMA data presented here suggest a ratio for the radius of (sub-)mm-sized dust grains to that of the molecular gas of $\lesssim$0.5, if we take the radial extent of the continuum and CO line emission at face value (see the discussion in Section 4.2.2). This is slightly larger than that predicted by the dust evolution models at $\sim$10^6 year (Birnstiel & Andrews 2014).

The presence of the inner cavity in the large dust grains in HD 97048 is indicative that some physical mechanism is in operation which is impeding radial drift and thus maintaining the population of large dust grains out to several hundred au. Quanz et al. (2012) do not discuss any evidence of gaps and substructure in the small grain populations in existing PDI images of HD 97048. If confirmed, this likely rules out photoevaporation as the origin of the cavity in the larger dust grains; however, van der Plas et al. (2009) do infer a cavity in the CO gas within the innermost 11 au using high-spectral-resolution vibrational line emission. That [O I] emission has been detected in the inner region (0.8–20 au, Acke & van den Ancker 2006) further supports the idea that CO gas is photodissociated by the strong far-UV flux from the star on small scales. Alternative theories include the presence of a planet or planetary system inside the cavity which creates a pressure gradient in the gas and traps the dust in a ring-like structure external to the location of the planet(s) (see, e.g., Pinilla et al. 2012a). The extracted intensity profile for HD 97048 also shows the presence of rings (at $\approx$50, 150, and 300 au) with associated gaps (at $\approx$100 and 250 au). If such substructure were caused by forming planets or companions *within* the protoplanetary disk, then this would also help to maintain a population of large dust grains out to several hundred au and increase the ratio of the radii of the (sub)mm-sized dust and molecular gas disks relative to that predicted by models which do not include the influence of planets. A recent reanalysis of ALMA Cycle 0 continuum emission from the disk around TW Hya (Hogerheijde et al. 2016) predicted the presence of one or more unseen embedded planets to explain the radial extent of (sub-)mm-sized dust grains; recent high (0″.3) to very high (0″.02) angular-resolution images of continuum emission from TW Hya confirm the presence of multiple rings and gaps which could be carved by the postulated unseen embedded planets (Andrews et al. 2016; Nomura et al. 2016; Tsukagoshi et al. 2016).

5.2. HD 97048 Versus HD 100546: Both Planet-hosting Disks?

HD 97048 and HD 100546 are both disk-hosting stars with a very similar spectral type. Multiple dust rings have been observed in the disk around HD 100546 with ALMA (Walsh et al. 2014; Pinilla et al. 2015), attributed to the presence of two massive companions: one orbiting within the cavity (<10 au, e.g., Acke & van den Ancker 2006; Brittain et al. 2014; Currie et al. 2015) and one, likely very young object, directly imaged at $\approx$50 au (Currie et al. 2014, 2015; Quanz et al. 2015). The extracted intensity profile for HD 97048 also shows evidence of substructure with peaks in emission at $\approx$50, 150, and 300 au and gaps in emission at $\approx$100 and 250 au. The cavity size for HD 97048 as determined from these data is $\approx$25 au which corresponds to the innermost radius of the FWHM of the innermost peak in emission (see Figure 6). We note here that
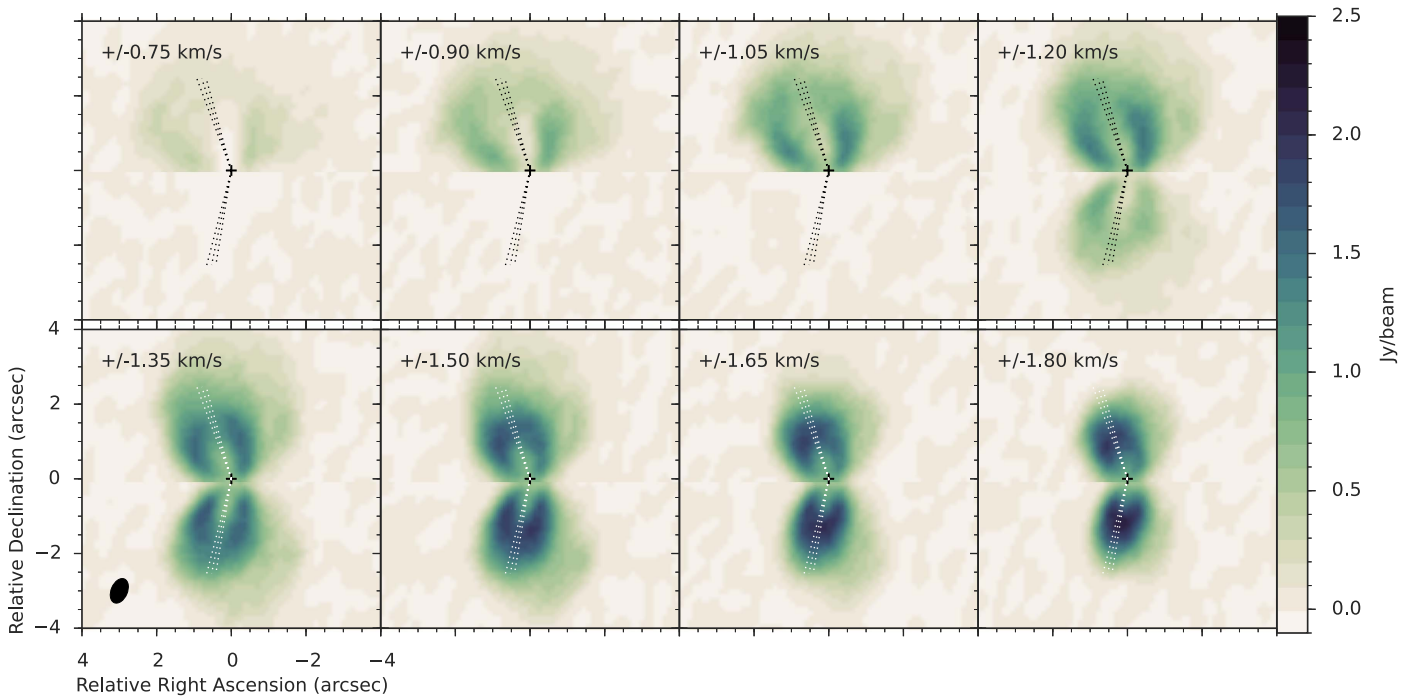
Figure 11. Channels maps showing the CO J = 3-2 (345.796 GHz) line emission with the positive and negative channels mirrored across zero relative decl. The black cross indicates the source position and the synthesized beam is shown in the bottom left-hand corner of the bottom left-hand panel. The dotted white and black lines show the projected angle of a surface inclined at 41° relative to the disk P.A. 3° with an opening angle (relative to the disk midplane) of 30°, 35°, and 40° (increasing from right to left).

the high signal-to-noise of the data (~1000) coupled with data analysis conducted in the visibility domain allows the extraction of substructure from the interferometric data on size scales which are smoothed over significantly in the resulting images.

In contrast with HD 100546, no observational evidence of a massive inner companion around HD 97048 yet exists, either in the disk continuum observations, or in the disk gas observations. However, elemental abundance measurements in the photosphere of HD 97048 hint that the gas-to-dust ratio of accreting material is large (750 ± 250) compared with the canonical interstellar medium value of ~100 (Acke & Waelkens 2004; Kama et al. 2015). Kama et al. (2015) hypothesize that this is a potential indirect determination of the presence of unseen inner planets/companions in Group I disks: the presence of planets in an inner gap or cavity impedes the flow of dust through the gaps whereas gas can flow freely, thereby locally increasing the gas-to-dust ratio in the accreting zone. The presence of an inner companion with an appreciable mass within the dust cavity will also excite spiral density waves which may be observable with future high-spatial observations at optical wavelengths.

Assuming that a single planet is responsible for clearing the inner cavity and trapping the (sub-)mm-sized dust beyond a radius of 25 au, one can estimate the mass and location of the planet (see, e.g., Crida et al. 2006; Dodson-Robinson & Salyk 2011; Pinilla et al. 2012a). Pinilla et al. (2012a) find that the dust accumulates at $\approx 7 r_H$ for planets with masses of 1–3 M_{Jup} and at $\approx 10 r_H$ for planets with mass >5 M_{Jup}, where r_H is the Hill radius ($r_H = r_p (M_p/3M_\star)^{1/3}$, where r_p and M_p are the radial location and mass of the planet and $M_\star$ is the stellar mass). In Figure 12, the light-green shaded region highlights the range of possible planet orbital locations and masses for a
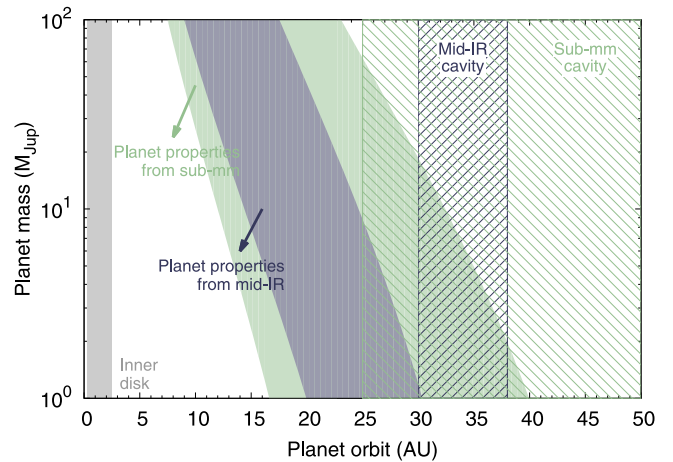
Figure 12. Plot showing the range of possible planet locations and masses for a single planet responsible for creating a dust trap between 25 and 50 au (light-green shaded area), and at 34 ± 4 au (dark-blue-shaded area). Also shown are the size of the optically thick inner dust disk (gray box, Maaskant et al. 2013), the cavity radius inferred from the ALMA data (light-green striped region, this work), and that inferred from mid-IR imaging (dark-blue striped region, Maaskant et al. 2013).

sub-mm dust ring located at radii between 25 and 50 au (as suggested in the ALMA data). Also plotted are the radial ranges of the optically thick inner disk (shaded gray region, 0.3–2.5 au, Maaskant et al. 2013), the cavity size inferred from the ALMA data (light-green striped region, 25–50 au, this work), and that inferred from the mid-IR imaging data (dark-blue striped region, 30–38 au, Maaskant et al. 2013). The dark-blue shaded region highlights the range of values when a cavity size of 34 ± 4 au is assumed (as inferred from the mid-IR
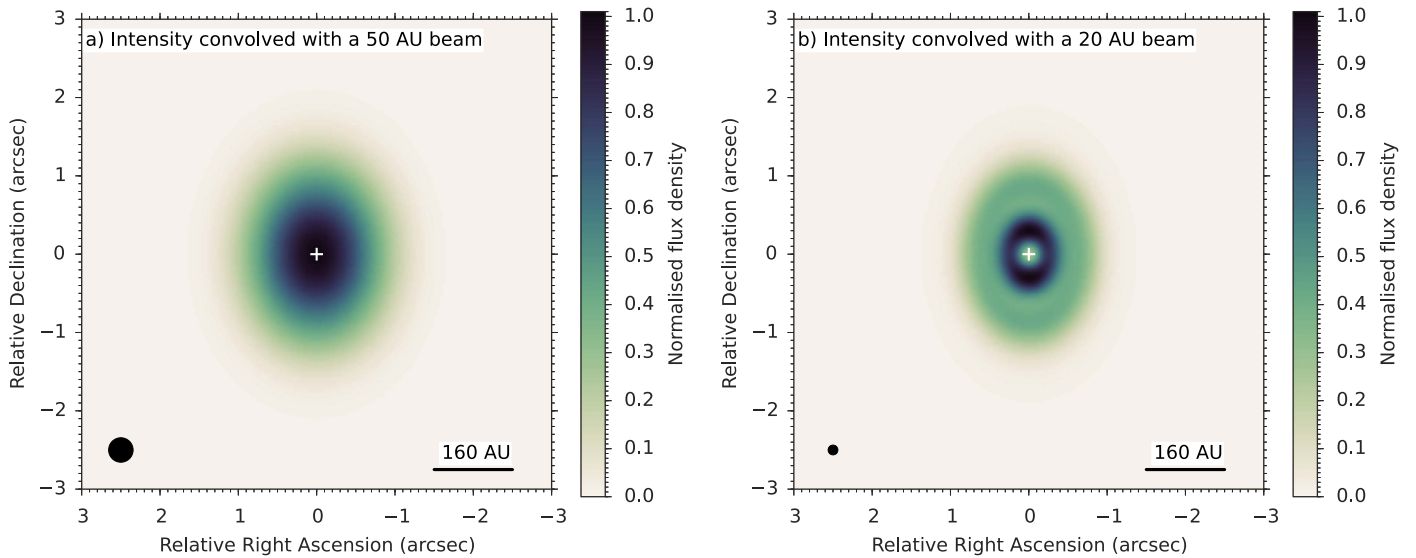
Figure 13. Normalized flux density using the best-fit intensity profile convolved with a 50 au beam (left-hand panel) and a 20 au beam (right-hand panel).

data). The range of planet locations and masses is set by the size of the gap carved in the gas ($\approx 5r_{\rm H}$, Dodson-Robinson & Salyk 2011) and the maximum dust gap size seen in the dust evolution models ($\approx 10r_{\rm H}$, Pinilla et al. 2012a).

This simple parameterization shows that a $1\,M_{\rm Jup}$ planet is able to create a dust trap at the required radius if it is located at 29 ± 12 au for a dust trap located between 25 and 50 au and 25 ± 5 au for a dust trap at 34 ± 4 au. However, such a low-mass planet is not able to open up a gap as wide as the full cavity inferred from both the ALMA data and the mid-IR imaging. It is more likely that a single planet has a mass $>10\,M_{\rm Jup}$, with planet/companion masses on the order of $100\,M_{\rm Jup}$ also possible. To date, no massive companion has been inferred from existing data on HD 97048, and no constraints on the mass of an as-yet unseen planet have been been determined (see, e.g., Acke & van den Ancker 2006; van der Plas et al. 2009; Brittain et al. 2014). That the cavity inferred in HD 97048 is larger than that for HD 100546, despite the lack of constraints on the presence or otherwise of a massive inner companion, is also intriguing. Very recently, Dong et al. (2015) presented results from 2D hydrodynamical models in which they show that multiple (four) low-mass ($1–2\,M_{\rm Jup}$) planets can open gaps on the order of a few tens of au in the mm-sized dust grains.

HD 97048 is yet another disk for which the dust emission at (sub-)mm wavelengths shows evidence of axisymmetric ring-like structures, here on spatial scales of around tens of au (Walsh et al. 2014; ALMA Partnership et al. 2015; Andrews et al. 2016; Nomura et al. 2016; Zhang et al. 2016). We predict that this substructure will be clearly evident in images of HD 97048 at higher spatial resolution ($\approx 10–20$ au, see Figure 13). There remains much debate in the literature on the origin of such axisymmetric substructure in protoplanetary disks including gaps and dust traps carved by forming planets (see, e.g., Dipierro et al. 2015; Pinilla et al. 2015; Rosotti et al. 2016), a change in dust opacity properties at the positions of snow lines (e.g., Banzatti et al. 2015; Zhang et al. 2015; Guidi et al. 2016; Okuzumi et al. 2016), and toroidal dust traps created by hydrodynamic or magnetohydrodynamic effects (see, e.g., Pinilla et al. 2012b; Lorén-Aguilar & Bate 2015; Ruge et al. 2016). To distinguish between each of the scenarios

requires observations of dust emission at multiple and well-separated frequencies to determine the radial dust size and density distribution (and dust opacity index) along with emission from optically thin gas tracers to determine the gas surface density. Planets will create deep gaps in the gas surface density as well as influencing the dust (note that this is dependent on the planet mass, see e.g., Rosotti et al. 2016), toroidal instabilities will create much shallower features in the gas surface density, and opacity changes at snow lines will affect only the dust emission and will have no effect on the gas. We note that the ringed substructure seen here has very recently been confirmed in scattered light images of HD 97048 taken with VLT/SPHERE (Ginski et al. 2016). An initial (and shallow) comparison of the data sets shows remarkable coincidence between the positions of the (sub-)mm peaks and gaps and those seen in scattered light. That such structure is seen in both small ($\approx \mu$m-sized) dust grains in the disk atmosphere and large ($\approx$mm-sized) dust grains in the disk midplane points toward a (proto)planetary system origin; however, further data, particularly to better constrain the gas structure, are needed for confirmation. Since this paper has been accepted for publication, ALMA Cycle 2 data of HD 97048, for which longer baseline data were available and imaged with a uv clip (>160 kλ), resulted in a beam of $0\rlap{.}''48 \times 0\rlap{.}''26$ (18°) and resolved the inner dust cavity ($<40 – 46$ au) and the bright dust ring at ≈ 150 au (van der Plas et al. 2016).

5.3. HD 97048: an Extremely Flared Disk?

The CO $J = 3$-2 data show that the molecular disk around HD 97048 extends to at least the same radius as the small dust grains imaged in scattered light (Doering et al. 2007), confirming that the scattered light does arise from a large circumstellar disk as opposed to a remnant circumstellar envelope. The CO data suffer from missing emission at and around the source velocity which could be due to foreground absorption and/or spatial filtering of background cloud emission; however, the data quality is sufficient to constrain the source velocity ($V_{\rm LSRK}$) to $4.65 \pm 0.075\,{\rm km\,s}^{-1}$. As discussed in Section 2, there exist limited data on emission from the outer regions of the molecular disk: most data are

spatially and spectrally unresolved and probe the inner warm/hot surface layers (Meeus et al. 2012, 2013; Fedele et al. 2013; van der Wiel et al. 2014). Hales et al. (2014) report the detection of CO $J = 3$-2 toward HD 97048 with APEX but identify the emission as arising from background material, because of an apparent offset in source velocity. Correcting the source velocity to $4.65\,\mathrm{km\,s^{-1}}$ in Figure 18 in Hales et al. (2014) shows that the emission does indeed arise from a disk in Keplerian rotation, albeit with a red wing which is significantly stronger than the blue wing and also with significant missing emission at the source velocity (as also seen in this work).

The data also show that the CO $J = 3$-2 emission arises from a layer with an opening angle (relative to the midplane) of $\approx 30°$–$40°$. This translates to a ratio, $z/r \approx 0.6$–0.8 (where z is the geometrical height and r is the disk radius), identifying HD 97048 as one of the most flared HAeBe disks known to date in ^{12}CO line emission, which is consistent with its SED classification as a (flared) Group I protoplanetary disk (Meeus et al. 2001; Acke et al. 2010). In comparison, Rosenfeld et al. (2013) derive an opening angle of $\approx 15°$ for the ^{12}CO-emitting surface in the disk around HD 163296 (similar to that also derived by De Gregorio-Monsalvo et al. 2013). This corresponds to $z/r \approx 0.3$ and is also consistent with its SED classification as a (flat) Group II protoplanetary disk (Meeus et al. 2001). Interestingly, Bruderer et al. (2012) reproduce the single-dish observations toward the Group I disk, HD 100546, with a model which suggests that the CO $J = 3$-2 emission arises from a layer deeper than that for HD 163296, at $z/r \approx 0.2$. Lagage et al. (2006) fit an intensity profile to the 8.6 μm PAH emission from HD 97048 using a power law, $z = (z_0/r_0)r^\beta$, where z_0 is the geometrical height of the emitting layer at r_0 and β is the power-law index (see also Chiang et al. 2001). They derive the following parameters: $z_0 = 51.3$ au and $\beta = 1.26$, for a fixed $z_0 = 135$ au. This translates to $z/r = 1.7$ at 300 au (roughly the spatial extent of the 8.6 μm PAH emission), confirming that the CO $J = 3$-2 emission arises from layer deeper in the disk than the far-UV-excited PAHs, as would be expected. Note that the PAH emission and CO $J = 3$-2 line emission both arise from layers in the disk at geometrical heights several times that of the expected gas pressure scale height.

5.4. Future Outlook

The data presented here are the first to spatially resolve the large disk around HD 97048 at (sub-)mm wavelengths. The data confirm the presence of a cavity in the large dust grains; however, higher spatial resolution data, ideally at multiple frequencies, are required to determine the depth of the gap in both dust and molecular gas and thus constrain the physical mechanism which is halting radial drift in the inner disk. High spatial resolution data will also shed light on the possible presence of a multiple planetary system composed of $\approx$ Jupiter-sized planets and will also confirm the multiple rings seen in the continuum emission in the current data. Finally, spatially resolved observations of multiple transitions of optically thin CO isotopologues will help to further constrain the location of the flared CO-emitting layer, and allow derivation of the temperature structure of the molecular gas. Quantification of the gas surface density will also allow further distinction between the various theories for the creation of the ring-like structures seen in the dust emission.

REFERENCES

Acke, B., Bouwman, J., Juhász, A., et al. 2010, ApJ, 718, 558
Acke, B., & van den Ancker, M. E. 2006, A&A, 449, 267
Acke, B., & Waelkens, C. 2004, A&A, 427, 1009
Alexander, R., Pascucci, I., Andrews, S., Armitage, P., & Cieza, L. 2014, in Protostars and Planets VI, ed. H. Beuther et al. (Tucson, AZ: Univ. Arizona Press), 475
ALMA Partnership, Brogan, C. L., Pérez, L. M., et al. 2015, ApJL, 808, L3
Andrews, S., Wilner, D. J., Espaillat, C., et al. 2011, ApJ, 732, 42
Andrews, S., Wilner, D. J., Hughes, M. A., et al. 2012, ApJ, 744, 162
Andrews, S., Wilner, D. J., Zhu, Z., et al. 2016, ApJL, 820, L40
Andrews, S. M., & Williams, J. P. 2007, ApJ, 659, 705
Banzatti, A., Pinilla, P., Ricci, L., et al. 2015, ApJL, 815, L15
Bary, J. S., Weintraub, D. A., Shukla, S. J., Leisenring, J. M., & Kastner, J. H. 2008, ApJ, 678, 1088
Beckwith, S. V. W., Sargent, A. I., Chini, R. S., & Guesten, R. 1990, AJ, 99, 924
Berger, J. P., & Segransan, D. 2007, NewAR, 51, 576
Birnstiel, T., & Andrews, S. M. 2014, ApJ, 780, 153
Blades, J. C., & Whittet, D. C. B. 1980, MNRAS, 191, 701
Briggs, D. S. 1995, PhD thesis, The New Mexico Institute of Mining and Technology
Brittain, S. D., Carr, J. S., Najita, J. R., Quanz, S. P., & Meyer, M. R. 2014, ApJ, 791, 136
Bruderer, S., van Dishoeck, E. F., Doty, S. D., & Herczeg, G. 2012, A&A, 541, A91
Carmona, A., van der Plas, G., van den Ancker, M. E., et al. 2011, A&A, 533, A39
Casassus, S., van der Plas, G., Perez, M. S., et al. 2013, Natur, 493, 191
Casassus, S., Wright, C. M., Marino, S., et al. 2015, ApJ, 812, 126
Chiang, E. I., Joung, M. K., Creech-Eakman, M. J., et al. 2001, ApJ, 547, 1077
Crida, A., Morbidelli, A., & Masset, F. 2006, Icar, 181, 587
Currie, T., Cloutier, R., Brittain, S., et al. 2015, ApJL, 814, L27
Currie, T., & Kenyon, S. J. 2014, AJ, 138, 703
Currie, T., Muto, T., Kudo, T., et al. 2014, ApJL, 796, L30
De Gregorio-Monsalvo, I., Ménard, F., Dent, W., et al. 2013, A&A, 557, A133
Dipierro, G., Price, D., Laibe, G., et al. 2015, MNRAS, 453, L73
Dodson-Robinson, S. E., & Salyk, C. 2011, ApJ, 738, 131
Doering, R. L., Meixner, M., Holfeltz, S. T., et al. 2007, AJ, 133, 2122
Dong, R., Zhu, Z., & Whitney, B. 2015, ApJ, 809, 93
Doucet, C., Habart, E., Pantin, E., et al. 2007, A&A, 470, 625
Draine, B. T. 2006, ApJ, 636, 1114
Dullemond, C. P., & Dominik, C. 2004, A&A, 417, 159
Espaillat, C., Muzerolle, J., Najita, J., et al. 2014, in Protostars and Planets VI, ed. H. Beuther et al. (Tucson, AZ: Univ. Arizona Press), 497
Fedele, D., Bruderer, S., van Dishoeck, E. F., et al. 2013, A&A, 559, A77
Flock, M., Ruge, J. P., Dzyurkevich, N., et al. 2015, A&A, 574, A68
Ginski, C., Stolker, T., Pinilla, P., et al. 2016, A&A, in press (arXiv:1609.04027)
Guidi, G., Tazzari, M., Testi, L., et al. 2016, A&A, 588, A112
Guilloteau, S., Dutrey, A., Piétu, V., & Boehler, Y. 2011, A&A, 529, A105
Gürtler, J., Schreyer, K., Henning, Th., Lemke, D., & Pfau, W. 1999, A&A, 346, 205

Hales, A. S., de Gregorio-Monsalvo, I., Montesinos, B., et al. 2014, AJ, 148, 47
Henning, Th., Buckert, A., Launhardt, R., Leinhert, Ch., & Stecklum, B. 1998, A&A, 336, 565
Henning, Th., Launhardt, R., Steincker, J., & Thamm, E. 1994, A&A, 291, 546
Hogerheijde, M., Bekkers, D., Pinilla, P., et al. 2016, A&A, 586, A99
Honda, M., Maaskant, K., Okamoto, Y. K., et al. 2012, ApJ, 752, 143
Hughes, A. M., Wilner, D. J., Calvet, N., et al. 2007, ApJ, 664, 536
Isella, A., Carpenter, J. M., & Sargent, A. I. 2009, ApJ, 701, 260
Isella, A., Pérez, L., & Carpenter, J. M. 2012, ApJ, 747, 136
Juhász, A., Bouwman, J., Henning, Th., et al. 2010, ApJ, 721, 431
Kama, M., Bruderer, S., Carney, M., et al. 2016, A&A, 588, A108
Kama, M., Folsom, C. P., & Pinilla, P. 2015, A&A, 582, L10
Lagage, P.-O., Doucet, C., Pantin, E., et al. 2006, Sci, 314, 621
Lorén-Aguilar, P., & Bate, M. R. 2015, MNRAS, 453, L78
Maaskant, K. M., Honda, M., Waters, L. B. F. M., et al. 2013, A&A, 555, A64
Mariñas, N., Telesco, C. M., Fisher, R. S., & Packham, C. 2011, ApJ, 737, 57
Martin-Zaïdi, C., Habart, E., Augereau, J.-C., et al. 2009, ApJ, 695, 1302
Martin-Zaïdi, C., Lagage, P.-O., Pantin, E., & Habart, E. 2007, ApJL, 666, L117
Meeus, G., Montesinos, B., Mendigutía, I., et al. 2012, A&A, 544, A78
Meeus, G., Salyk, C., Bruderer, S., et al. 2013, A&A, 559, A84
Meeus, G., Waters, L. B. F. M., Bouwman, J., et al. 2001, A&A, 365, 476
Menu, J., van Boekel, R., Henning, Th., et al. 2015, A&A, 581, A107
Nomura, H., Tsukagoshi, T., Kawabe, R., et al. 2016, ApJL, 819, L7
Okuzumi, S., Momose, M., Sirono, S., Kobayashi, H., & Tanaka, H. 2016, ApJ, 821, 82
Patil, A., Huard, D., & Fonnesbeck, C. J. 2010, J. Stat. Soft, 35, 1
Phillips, N. M. 2010, PhD thesis, Univ. Edinburgh
Pineda, J., Quanz, S., Meru, F., et al. 2014, ApJL, 788, L34
Pinilla, P., Benisty, M., & Birnstiel, T. 2012a, A&A, 545, A81
Pinilla, P., Birnstiel, T., Ricci, L., et al. 2012b, A&A, 538, A114
Pinilla, P., Birnstiel, T., & Walsh, C. 2015, A&A, 80, A105
Quanz, S. P., Amara, A., Meyer, M. R., et al. 2015, ApJ, 807, 64
Quanz, S. P., Birkmann, S. M., Apai, D., Wolf, S., & Henning, Th. 2012, A&A, 538, A92

Regály, Zs., Sándor, Zs., Csomós, P., & Ataiee, S. 2013, MNRAS, 433, 2626
Rice, W. K. M., Armitage, P. J., Wood, K., & Lodato, G. 2006, MNRAS, 373, 1619
Rosenfeld, K. A., Andrews, S. M., Hughes, A. M., Wilner, D. J., & Qi, C. 2013, ApJ, 774, 16
Rosotti, G. P., Juhász, A., Booth, R. A., & Clarke, C. 2016, MNRAS, 459, 2790
Ruge, J. P., Flock, M., Wolf, S., et al. 2016, A&A, 590, A17
Sememov, D., Pavyluchenkov, Ya., Henning, Th., Wolf, S., & Launhardt, R. 2007, ApJL, 673, L195
Strom, K. M., Strom, S. E., Edwards, S., Cabrit, S., & Skrutskie, M. F. 1989, AJ, 97, 1451
Tsukagoshi, T., Nomura, H., Muto, T., et al. 2016, ApJL, 829, L35
van Boekel, R., Waters, L. B. F. M., Dominik, C., et al. 2004, A&A, 418, 177
van den Ancker, M. E., de Winter, D., & Tjin A Djie, A. 1998, A&A, 330, 145
van der Marel, N., Pinilla, P., Tobin, J., et al. 2015, ApJL, 810, L7
van der Marel, N., van Dishoeck, E. F., Bruderer, S., et al. 2013, Sci, 340, 1199
van der Plas, G., van den Ancker, M. E., Acke, B., et al. 2009, A&A, 500, 1137
van der Plas, G., van den Ancker, M. E., Waters, L. B. F. M., & Dominik, C. 2015, A&A, 574, A75
van der Plas, G., Wright, C. M., Ménard, F., et al. 2016, A&A, in press (arXiv:1609.02488)
van der Wiel, M. H. D., Naylor, D. A., Kamp, I., et al. 2014, MNRAS, 444, 3911
van Kerckhoven, C., Tielens, A. G. G. M., & Waelkens, C. 2002, A&A, 384, 568
van Leeuwen, F. 2007, A&A, 474, 653
Visser, R., van Dishoeck, E. F., & Black, J. H. 2009, A&A, 503, 323
Walsh, C., Juhász, A., Pinilla, P., et al. 2014, ApJL, 791, L6
Waters, L. B. F. M., & Waelkens, C. 1998, ARA&A, 36, 233
Weidenschilling, S. J. 1997, MNRAS, 180, 57
Whipple, F. L. 1972, From Plasma to Planet (New York: Wiley-Interscience) 211
Wright, C. M., Maddison, S. T., Wilner, D. J., et al. 2015, MNRAS, 453, 414
Zhang, K., Bergin, E. A., Blake, G. A., et al. 2016, ApJL, 818, L16
Zhang, K., Blake, G. A., & Bergin, E. A. 2015, ApJL, 806, L7